Supporting Information

Ultrafast Glimpses of the Excitation Energy-Dependent Exciton Dynamics and Charge Carrier Mobility in Cs_2SnI_6 Nanocrystals

Gurpreet Kaur[1], Ayushi Shukla[1,§], Arijit Sinha[2,§], Koyendrila Debnath[2,§], Kaliyamoorthy Justice Babu[1], Himanshu Bhatt[1], Umesh V. Waghmare[2]* and Hirendra N. Ghosh[1,3,]*.

[1] Institute of Nano Science and Technology, Knowledge City, Sector 81, SAS Nagar, Punjab-140306, India

[2]Jawaharlal Nehru Centre for Advanced scientific Research, Theoretical Sciences Unit,

Bangalore 560064, India

[3]Radiation and Photochemistry Division, Bhabha Atomic Research Centre (BARC), Mumbai

-400085, India.

[§]-The authors contributed equally

TABLE OF CONTENTS:

1. Synthesis procedure for Cs_2SnI_6 Nanocrystals (NCs)

Chemicals required: Cesium Carbonate (Cs_2CO_3, 99 % trace metals basis), Tin (IV) Iodide (SnI_4), Oleic Acid (OA), Octadecence (ODE), Oleylamine (OLA) and n-hexane were purchased from Sigma Aldrich and employed for synthesis without any further purification.

Preparation of Cs- Oleate: 0.8g of Cs_2CO_3 together with 10 mL of ODE and 1.5 mL of OA were loaded in a 50 mL three-neck Round Bottomed Flask (RBF).To begin with, the reaction precursors were initially heated to 100° C while being degassed under vacuum to get rid of any moisture and then the reaction temperature was raised to 140° C while the solution was continuously purged with N_2. The successful formation of Cs- Oleate was indicated by the complete dissolution of Cs_2CO_3. Since at room temperature, Cs- Oleate precipitates out of ODE, therefore every time prior to usage for NC synthesis, the solution needs to be preheated to ~100ºC.

Synthesis of Cs_2SnI_6 NCs: 0.12 g of SnI_4, 0.7 mL OLA, 0.7 mL OA and 7 mL ODE were loaded together into a 25 ml RBF for the preparation of tin precursor. The solution was then heated to 100º C while being degassed for 1h. Following this, the reaction temperature was elevated to 210 º C with continuous N_2 purging. 0.5mL of the preheated Cs-Oleate was then injected into this reaction mixture while the solution was vigorously stirred. The transparent yellow solution turned deep orange, implying the successful formation of Cs_2SnI_6 NCs. The reaction was then quenched using an ice-water bath after 10s of injection. The obtained product was centrifuged twice to remove any unreacted precursors and the final precipitate was then dispersed in n-hexane for further characterisations.

2. Crystallographic characterisations: X-Ray Diffraction (XRD) pattern

The peaks obtained in the XRD pattern hold fair agreement with the cubic structure of Cs_2SnI_6 (JCPDS No. 51-0466) justifying the crystallisation of the synthesised NCs in $Fm\bar{3}m$ crystal structure with an edge parameter of 11.65Å.

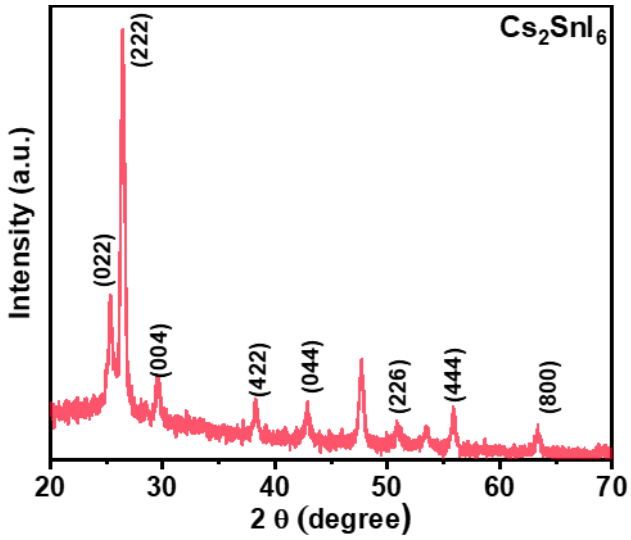

Figure S1 XRD pattern of the as-synthesized Cs_2SnI_6 NCs spin coated over glass substrate.

3. Morphological characterisations: Transmission Electron Microscopy (TEM) images

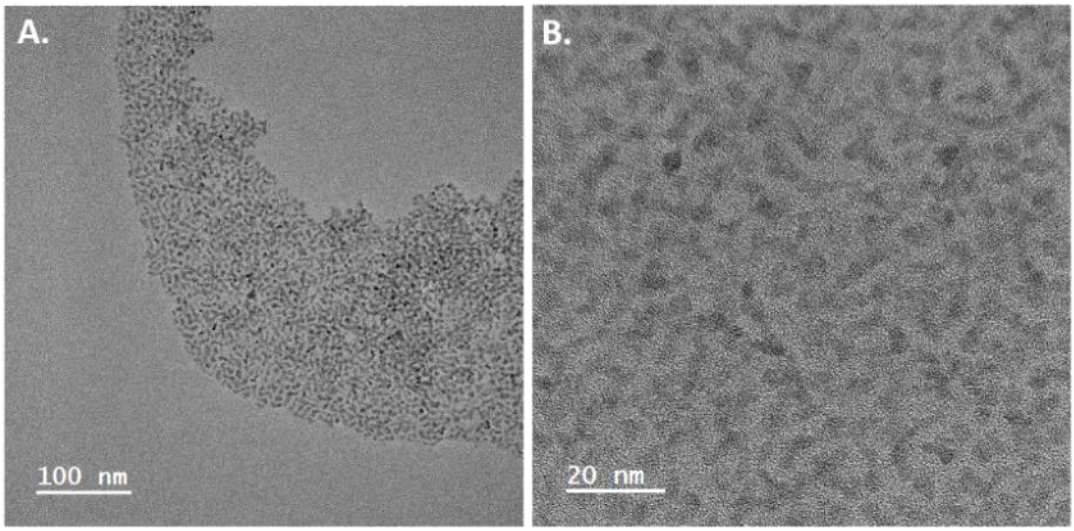

Figure S2 (A, B) Large area TEM images of the synthesised Cs_2SnI_6 NCs.

4. Computational details

Our *first-principles* calculations are based on density functional theory (DFT) as implemented in VASP (Vienna Ab initio Simulation Package) with interactions between valence electrons and ion cores treated using projector-augmented-wave (PAW) potentials.[1–4] Exchange correlation energy has been treated using the PBEsol,[5] a version of Perdew-Burke-Ernzerhof (PBE) parametrized functional of a generalized gradient approximation (GGA).[6] We used an energy cutoff of 520 eV to truncate the Kohn-Sham (KS) wavefunctions. Brillouin zone integrations were sampled on Γ-centered uniform mesh of 8x8x8 k-points in calculations of $Fm\bar{3}m$ (225)[1] phase. A comparison between Figure S3A and Figure S3B reveals that Cs_2SnI_6 in $Fm\bar{3}m$ structure can be obtained from 2x2x2 cubic supercell of $CsSnI_3$ (space group: $Pm\bar{3}m$), by removing alternating Sn atoms (from the center of the $[SnI_6]^{2-}$ orange octahedra in Figure S3A). Hence, the corner-shared $[SnI_6]^{2-}$ octahedra in perovskite structure of $CsSnI_3$ become isolated in Cs_2SnI_6 (Figure S3B). We aided convergence to self-consistency by smearing the discontinuity in occupation numbers of electronic states with broadening temperature of k_BT = 0.04 eV. A self-consistent solution of the KS equation is obtained iteratively until the total energy is converged within 10^{-8} eV/cell. Structures were optimized through minimization of energy until the magnitude of each component of Feynman-Hellman force is smaller than 10^{-3} eV/Å and each component of the stress tensor is less than 10^{-2} GPa. We have used PHONOPY code to convert the representation of structure based on conventional unit cell to that based on the primitive cell of $Fm\bar{3}m$ (225).[7,8] The PBEsol line of GGA-PBE exchange-correlation functional tends to underestimate electronic energy band gap for Cs_2SnI_6. The hybrid functional, which mixes it with a nonlocal Hartree–

[1] The number in the parenthesis after the space group symbol is space group number.

Fock exchange, gives more accurate electronic band energies and gaps of solid materials. Therefore, we chose HSE06[9] hybrid functional in this study (with standard values of mixing fraction α = 0.25 of the exact Hartree–Fock exchange with GGA and a screening parameter ω = 0.2 $Å^{-1}$). To obtain optical absorption spectrum of Cs_2SnI_6 in $Fm\bar{3}m$ (225) structure, we have used uniform mesh of 18x18x18 k-points to sample the Brillouin zone and calculated frequency dependent real and imaginary part of dielectric constant. Optical absorption coefficient is determined using the following relation:

$$\alpha(\omega) = \frac{\sqrt{2}\cdot\omega}{c}\left(\sqrt{(\varepsilon_1^2+\varepsilon_2^2)}-\varepsilon_1\right)^{\frac{1}{2}} \qquad \text{Eq. S1}$$

In equation (S1), $\alpha(\omega)$, ε_1 and ε_2 are frequency dependent absorption coefficient, real and imaginary parts of dielectric constant.

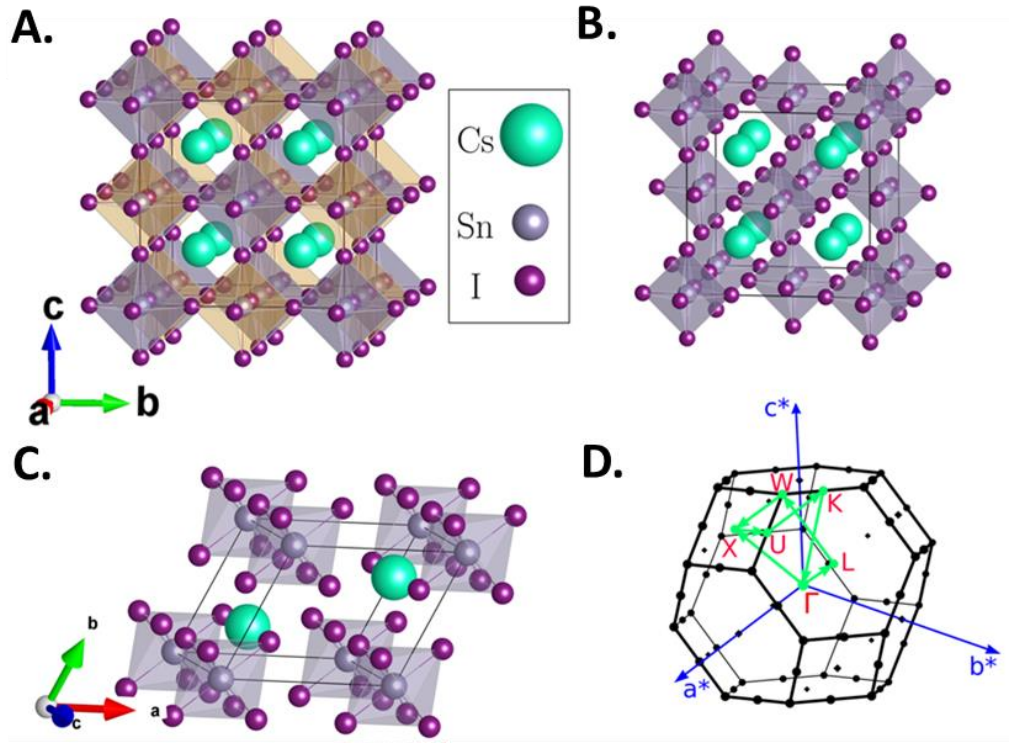

Figure S3 (A) 2x2x2 supercell of $CsSnI_3$ in cubic perovskite $Pm\bar{3}m$ phase, **(B)** Cs_2SnI_6 in $Fm\bar{3}m$ phase obtained with removal of alternating Sn atoms (centered in yellow octahedra in **(A)**). Primitive unit cell of **(C)** Cs_2SnI_6 which contains 1 formula unit (black lines in each figure defines unit cell). **(D)** Brillouin zone and high symmetry paths (shown in green solid line) of Cs_2SnI_6 in $Fm\bar{3}m$ phase shown in **(C)**.

We have used post-processing tool vaspkit[10] to obtain Figure 2 (A) electronic structure, (B) orbital projected density of states, (C) transition dipole moment (TDM) matrices between states from valence bands and conduction bands and (D), (E) visualization of electronic wavefunctions of frontier states at valence band maximum (VBM) and conduction band minimum (CBM). VESTA[11] package has been used to visualize the structures.

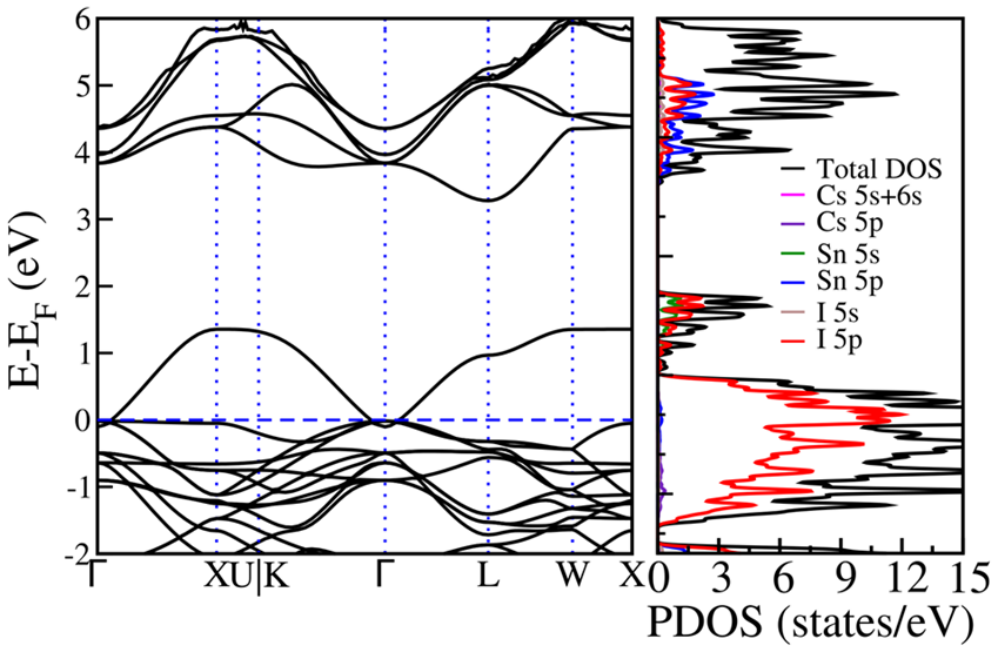

Figure S4 Electronic band structure using PBEsol functional which underestimates the electronic band gap and shows Cs_2SnI_6 as a metal.

We have used PHONOPY to transform structure from conventional to primitive unit cell of Cs_2SnI_6T. The transformation matrix used in this case is the following:

$$\begin{bmatrix} 0.0 & 0.5 & 0.5 \\ 0.5 & 0.0 & 0.5 \\ 0.5 & 0.5 & 0.0 \end{bmatrix} \quad \text{Eq.S2}$$

5. Tauc plot and Ultraviolet Photoelectron Spectroscopy (UPS) analysis

Estimating the Fermi level position from Ultraviolet Photoelectron Spectroscopic (UPS) measurements. The theoretical calculations have been performed presuming the system to be pristine, free of any intrinsic defects and vacancies. Nevertheless there are several reports which demonstrate that due to the easy formation of V_I (iodine vacancy) and Sn_I (tin interstitial) donors during the synthesis process, Cs_2SnI_6 intrinsically exhibits properties analogous to an intrinsic n-type semiconductor.[12,13] In a very recent experimental finding, Noh and co-workers found the Fermi level in Cs_2SnI_6 lying very close to the CBM edge (only 0.02 eV below the CBM).[14] Therefore, it may not be reasonable to make a straightforward remark regarding the occupancy of CB by analysing the position of the Fermi level deduced from theory. But then in order to address the photo-physical processes, understanding the positioning of these excitons is not sufficient. It is also essential to know that whether the states constituting CB that are involved in the excitonic transition are filled with electrons or are vacant. For this realisation, the knowledge of the positioning of the Fermi level (E_f) *w.r.t.* the CB edge (C.B.) is crucial. Therefore, we performed Ultraviolet Photoelectron Spectroscopic (UPS) measurements which provided the position of the band edge levels and the Fermi level relative to vacuum. The band level diagram presented in Figure S5C demonstrates all the energy levels obtained from the combined UPS and Tauc Plot analysis. From the Tauc plot Figure S5 A, the band gap (E_g) is estimated to be 1.71 eV. The binding energy plot yields the secondary cut-off energy edge $E_{Cut\text{-}off}$ at 17.5 eV (Figure S5 B) and then in accordance with the equation, E_f = 21.22 eV (He I)-E_{CutOff},[5] the fermi energy level (E_f) is determined close to 3.72 eV. Further to extract the VB edge (E_v), we linearly extrapolated the low energy binding region (E_v - E_f) which yields E_v as 5.82 eV. Thereby the CB edge is found to lie at 4.11 eV (E_v + E_g).

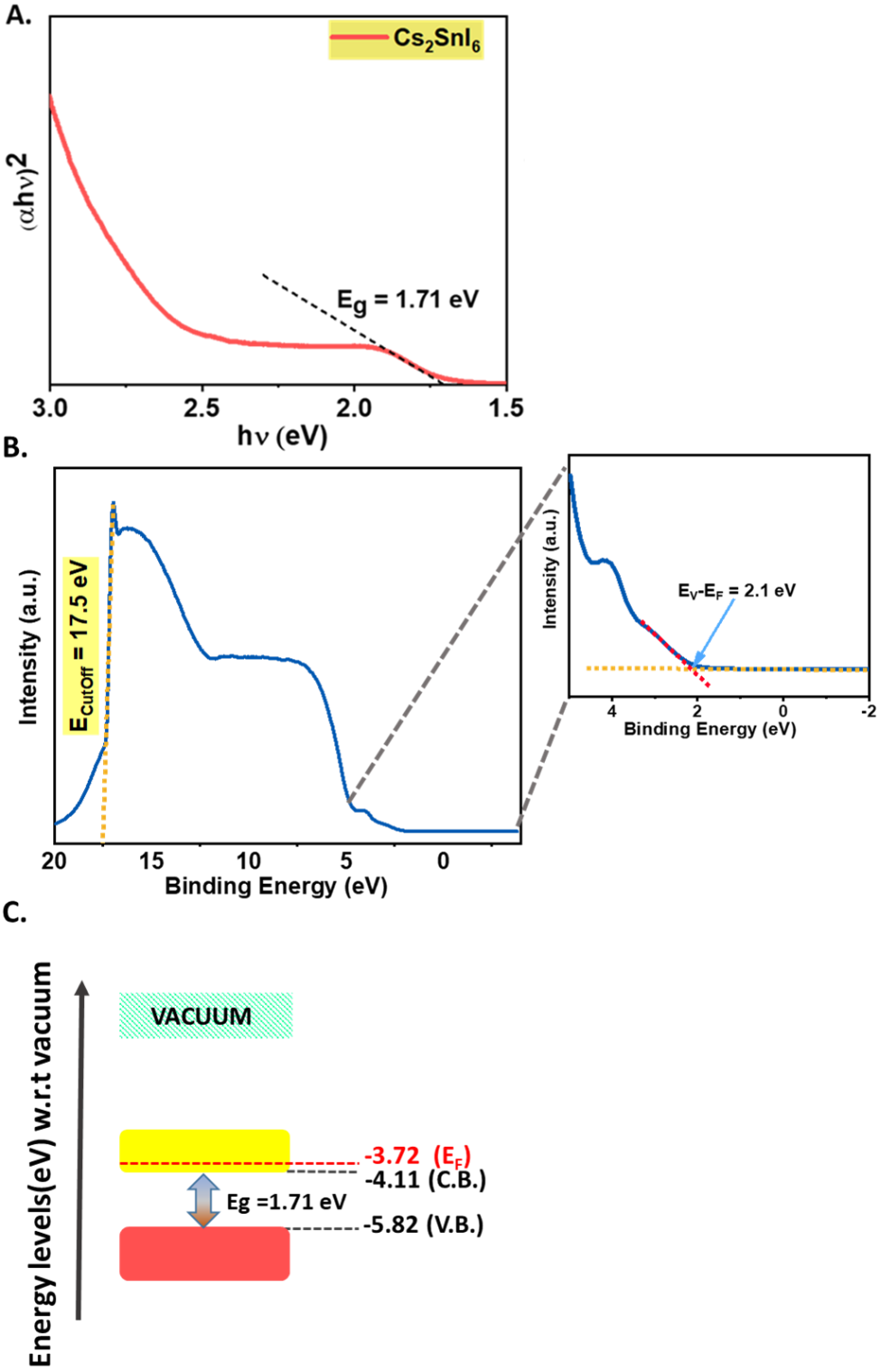

Figure S5 (**A)** Tauc plot used for the estimation of the energy band gap (E_g), obtained from steady-state absorption keeping in consideration that Cs_2SnI_6 is a direct band gap material, **(B)** UPS plot in the high binding energy regime employed for the estimation of E_f from the secondary cut-off energy. The zoomed region shows the linear extrapolation of the low energy region of the plot yielding "$E_v - E_f$", **(C)** The band level diagram displaying the band levels of Cs_2SnI_6 after summarising the collective results obtained from the UPS investigations and Tauc plot.

It is previously reported that in Cs_2SnI_6, CB is typically spread over a wide energy range of roughly 1.35 eV.[11] Considering this along with the inferences drawn from the UPS analysis conducted in the present work reveals that the Fermi level in Cs_2SnI_6 passes through CB, directly suggesting that Cs_2SnI_6 is a degenerate n-type semiconductor material. Thereby, CB is not an absolutely vacant band. Instead, the states constituting the band lying below E_f in close proximity with the CBM edge are filled with electrons, thus making this band partially filled but only near the edge.

6. Field Emission Scanning Electron Microscopy (FE-SEM)

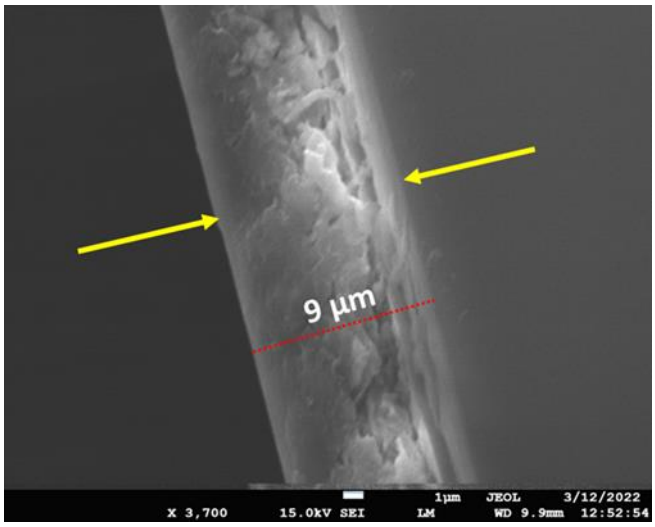

Figure S6 Field Emission Scanning Electron Microscopy (FE-SEM) image displaying the thickness of the as-deposited Cs_2SnI_6 NCs over the quartz substrate.

7. Calculation for the injected carrier density

Eq. S3 is used to estimate the total number of injected photo charge carriers "n".[15]

$$n = \frac{A(E) \text{ x I}}{t \text{ x E}} \qquad \text{Eq. S3}$$

where A(E) denotes the absorption intensity (optical density) measured at the pump excitation energy (E), I denotes the input laser flux, and t is the deposited sample thickness.

In the present work,

For 2eV excitation,

Incident laser pump power = 200µW

Since our pump beam diameter is 250 µm, so the equivalent energy flux I = 400 µJ/cm^2

The thickness (t) of the as-deposited film is determined using cross-sectional FESEM investigations (Figure S6) = 9µm,

A(E) measured at the pump excitation energy (E) of 2 eV =1.

As a result, by substituting all these quantities in Eq.S1 the number of injected charge carriers (n) at this energy is calculated to be around 1.4 x 10^{18} cm^{-3}.

For 4 eV excitation, since A (E) is measured to be 3.4. So in order to maintain the same carrier density at 4 eV as well, we reduced the laser intensity from 400 μJ/cm^2 to 240 μJ/cm^2 (120 μW).

Similarly for other pump energies as well, by modulating the laser intensity we ensured that the injected charge carrier density remains identical.

8. Calculation for average number of excitons

We chose to work with this particular fluence that fundamentally corresponds to ~ 10^{14} - 10^{15} photons/cm^2 depending on the incident pump energy. This fluence conforms to the situation when only one exciton is expected per nanocrystal (<N> <1).This claim is fortified by the calculations performed for deducing the average number of excitons per nanocrystal (<N>):[16]

$$\langle N \rangle = \sigma . J \qquad \text{Eq. S4}$$

Here, σ implies the NC surface area (cross section) and J stands for the average number of photons/cm^2.

Further, the NC cross section can be mathematically expressed as:

$$\sigma = 4/3\ \pi \left| f \right|^2 \alpha R^3 \qquad \text{Eq. S5}$$

where R is the NC radius as estimated from TEM, α is the bulk absorption coefficient and $\left| f \right|^2$ is the coefficient for local field effect (~0.25).

For Cs_2SnI_6,[17–19] $\alpha \sim 10^4 cm^{-1}$

Average NC radius obtained from TEM images (R) = 2 nm

Substituting all the values in Eq.S5 yields $\sigma = 4/3 \times 3.14 \times 0.25 \times 10^4 \times (2)^3 \times (10^{-21})$

$$\sigma = 8.37 \times 10^{-17}\ cm^2$$

Average number of photons incident per cm^2 (J) (2eV excitation) = 1.2 x 10^{15} /cm^2

Therefore , $\langle N \rangle = \sigma . J = 8.37 \times 10^{-17} \times 1.2 \times 10^{15} = 0.1$

For entire range of pump energies, the absorption coefficient α varies between 3.5 – 4.5 x $10^4 cm^{-1}$ (σ - 2.9 x 10^{-16} – 3.7 x 10^{-16}) and J varies between 4.8 x 10^{14}/cm^2 (4 eV Pump) to 1.2 x 10^{15}/cm^2 (2eV pump). But one thing that remains certain is that the product of these parameters *i.e.* <N> strictly remains restricted to < 1.

Therefore it can be safely stated that our investigations ensure single exciton conditions.

9. Transient absorption results collected in the visible domain

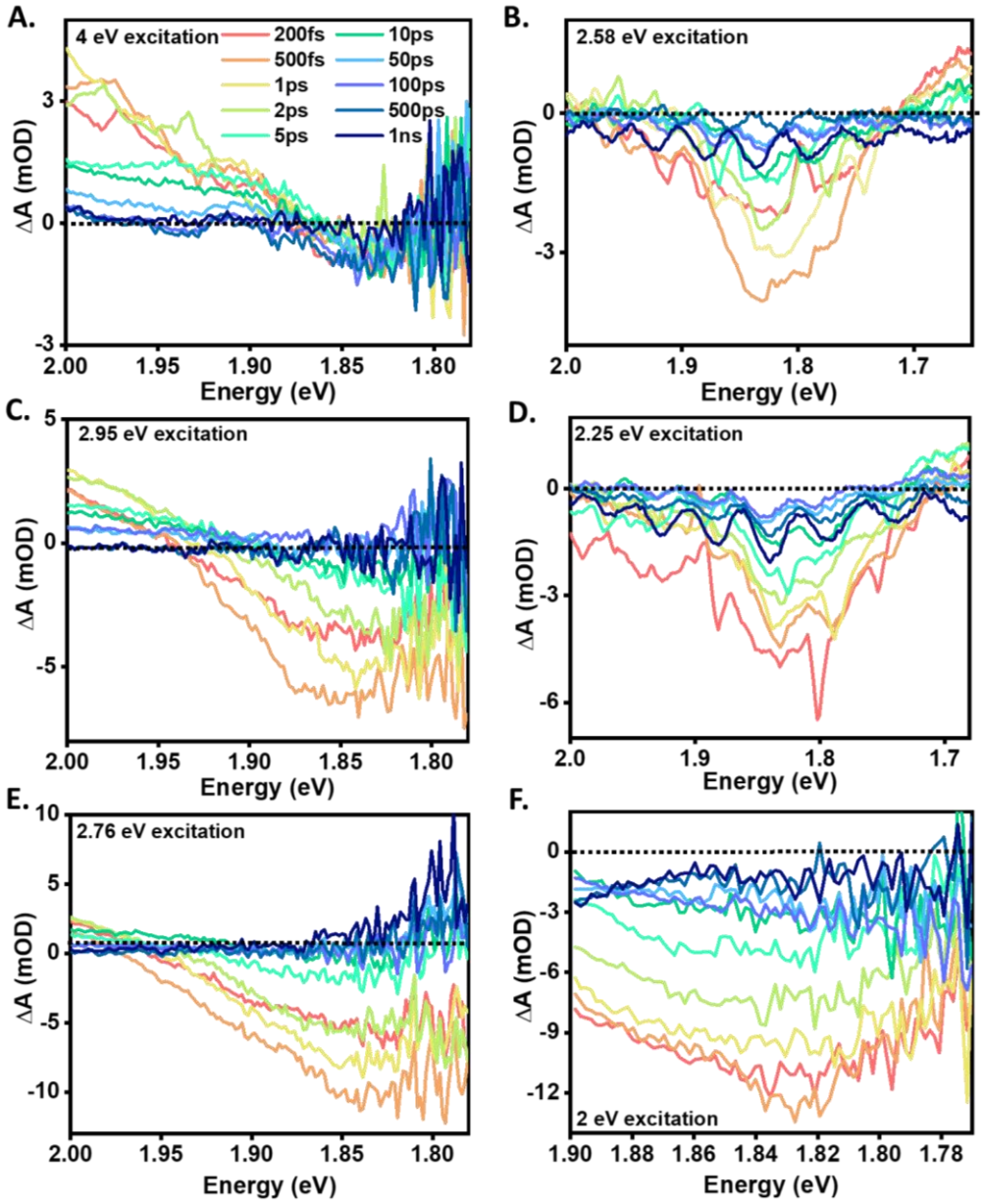

Figure S7 TA spectral responses recorded in the visible probe region upon exciting the Cs_2SnI_6 NCs with different pump energies.

10. Explanation for the absence of transient bleach corresponding to B-exciton – the case of 4 eV excitation

One plausible reason for such an observation may be that the bleach intensity corresponding to B-exciton is relatively very weak in comparison to the positive signal thus causing positive signal to dominate. Such types of strong broad positive feature can arise from the photo-induced absorption (PIA) of probe which carries the excited carriers to further higher-lying electronic states.[20] The other equally possible reason that can be held liable for the absence of an anticipated bleach is the ultrafast transfer of the carriers constituting this bleach to some other electronic states lying elsewise in the k-space.[21] This second possibility appears to be

more appropriate in this present case. The bleach due to C-exciton is unusually wide (wider than that for lower energy excitations) and stretched towards the low energy end, indicating a possible its overlap with B-exciton bleach. Because the intensity of this B exciton bleach may be so low due to the transfer process being so fast and efficient, we fail to see the characteristic clearly. This is further validated by the observations made in the later sections of the transient data analysis in the main text.

11. The origin of the low energy positive signal at 1.65 eV

It is frequently seen that the low energy positive signal observed towards the red side of the lowest energy bleach in metal halide perovskite structures is due to biexciton formation in the system. Biexciton essentially refers to a four particle bound and stable quasi- system constituted by two excitons. The inception of biexciton in a pump- probe experiment can normally take place under two circumstances. It can be either a result of Coloumbic interaction existing between two pump generated excitons (in case if the incident pump flux is sufficient enough to generate atleast two excitons per nanocrystal) or it can also be an outcome of the Coulombic interaction existing between an exciton generated by the pump incidence and another by probe absorption. Under the present experimental conditions, it is warranteed that the former situation cannot rise since the fluence conditions deployed ensure that there is only single exciton generation feasible. This is certified by the calculations performed to conclude the number of excitons that are photogenerated per nanocrystal upon pump irradiation (provided in section 8 above).

Regarding the possibility of the probe induced biexciton formation : the characteristic signature of biexciton in transient absorption spectroscopy is initial appearance of a positive signal towards the low energy end of the ground state bleach which is then later replaced by a negative signal due to biexciton decay into a single exciton through Auger recombination. However, in our work, the positive signal probed at the low energy end does not transform to a negative bleach, as it should have if it was due to biexciton formation (Figure S8). Besides this, it is widely reported that in situations whenever there is biexciton formation, there is a an initial red shift observed at the band edge exciton bleach position due to band gap renormalisation followed by no further change in spectral position of the bleach once the biexciton decays into single exciton.[22,23] But we didn't observe any such time dependent shift in the ground state bleach band edge position over the entire time range monitored. Since the positive signal rather than transforming into a negative signal, returns simply to zero, therefore the probable origin of this positive signal at 1.65 eV is due to initial trapping and then detrapping of the carriers in the defect states. Nevertheless, understanding the exact origin of this positive signal is in itself a complete topic to look into and requires an extensive analysis. Our interest in this work is more inclined towards exciton dynamics.

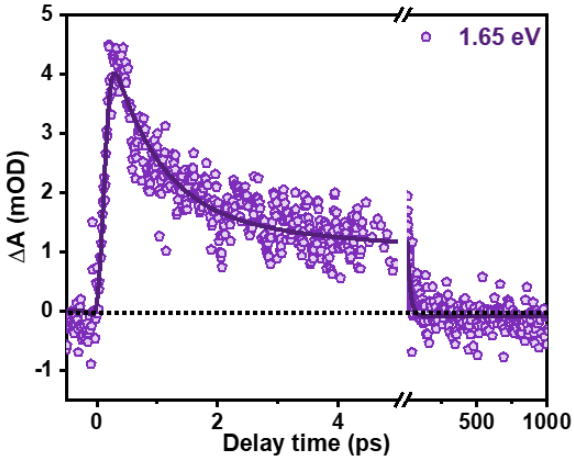

Figure S8 Transient kinetics of the positive signal probed at 1.65 eV.

12. Fitting parameters

Table S1. Fitting parameters for A exciton bleach growth dynamics

Excitation pump energy (eV)	*Bleach growth time τ_g (fs)*
4	700
2.95	550
2.75	540
2.58	440
2	450

Table S2. Fitting parameters for dynamics for the three bleaches under three different pump excitations

Table S2 A. Pump energy = 4 eV

Exciton bleach	*Growth time τ_g (ps)*	*Decay time τ_{d1} (ps)*	*Decay time τ_{d2} (ps)*	*Decay time τ_{d3} (ns)*
A	0.7(100%)	4.72 (-80.2%)		>1 (-19.8%)
C	0.35(100%)	10.1(-74%)	210 (-20%)	>1 (-6%)

Table S2 B. Pump energy = 2.95 eV

Exciton bleach	*Growth time τ_g (ps)*	*Decay time τ_{d1} (ps)*	*Decay time τ_{d2} (ns)*
A	0.55(100%)	61.9 (-92.5%)	>1 (-7.5%)
C	0.35(100%)	39 (-79%)	>1 (-21%)

Table S2 C. Pump energy = 2.76 eV

Exciton bleach	*Growth time τ_g (ps)*	*Decay time τ_{d1} (ps)*	*Decay time τ_{d2} (ns)*
A	0.54(100%)	63.4 (-100%)	> 1 (100%)
B	<0.1 (100%)	7.1 (-100%)	> 1 (100%)
C	0.8(100%)	120.3 (-100%)	> 1 (100%)

Table S2 D. Pump energy = 2.58 eV

Exciton bleach	*Growth time τ_g (ps)*	*Decay time τ_{d1} (ps)*	*Decay time τ_{d2} (ns)*
A	0.420(100%)	9(-100%)	>1 (100%)
B	0.220 (100%)	18.6 (-88.75%)	>1 (-11.25%)

Table S2 E. Pump energy = 2 eV

Exciton bleach	*Growth time τ_g (ps)*	*Decay time τ_{d1} (ps)*	*Decay time τ_{d2} (ns)*
A	0.450(100%)	11.4(-60%)	>1 (-40%)
B	0.330 (100%)	13.7(-95%)	>1 (-5%)

13. Steady state Terahertz (THz) waveforms

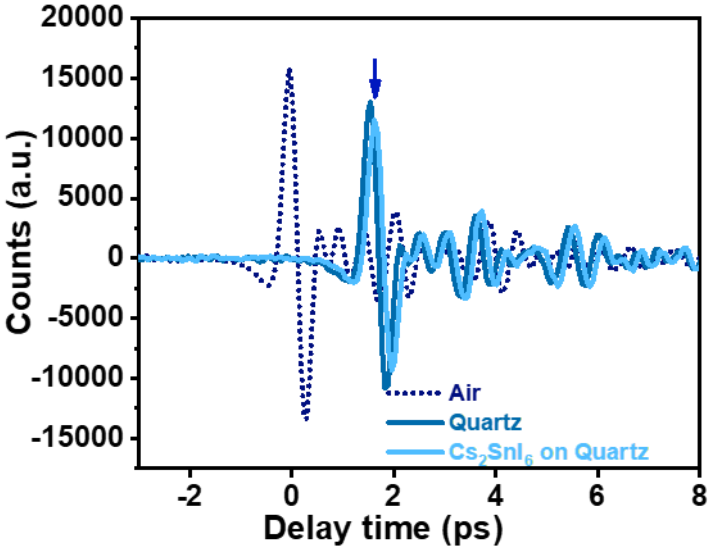

Figure S9 THz-TDS waveform transmitted through air, quartz and Cs_2SnI_6 spin coated over quartz substrate.

14. Experimental section: Instrumentation details

The crystal structure of as-synthesized NCs was investigated using a powder X-ray diffractometer (BRUKER D8 ADVANCE) with Cu-Kα radiation (λ = 1.542 Å) and a scanning angle (2θ) range of 20º-70º. The acquired pattern was matched with JCPDS card number 51-0466 from the International Centre for Diffraction Data's Powder Diffraction File database. Shimadzu UV-2600 UV-vis spectrophotometer was used to collect the optical absorption spectra. PL data was collected using an Edinburgh FS5 spectroflourometer. TEM was performed using a JEOL 2100 microscope with a 200 kV accelerating voltage. UPS measurements of both the samples were performed using XPS/ ESCALAB250Xi, Thermo Fisher Scientific, America.

Femtosecond Transient Absorption spectroscopy setup:

The experimental setup for the collection of differential absorption data employs a Ti: Sapphire regenerative amplifier based femtosecond laser system (Astrella, Coherent systems, Pulse energy 5mJ, fundamental wavelength 800 nm, pulse width 35 fs) and Helios Fire spectrometer, as mentioned in our previous article.[15] A dichroic beam splitter (R: T = 90:10) divides the beam from the main laser head (with a repetition rate of 1 kHz) into two components: pump and probe beam. Using an Optical Parametric Amplifier, the reflected component, i.e. the pump, may be tuned to any desired excitation wavelength (within the system restrictions) (OperA SOLO). The pump intensity may be modulated using a variable neutral density filter. The other component, the probe beam, travels via a computer-controlled delay stage and onto a CaF_2 window to produce a white light continuum. The pump beam frequency is decreased to 500 Hz using a synchronised chopper in order to calculate the absorbance change in two subsequent probe pulses, which may be expressed as

$$\Delta \mathbf{A} = \mathbf{A}^{\mathbf{Probe}}_{\mathbf{(PUMP,ON)}} - \mathbf{A}^{\mathbf{Probe}}_{\mathbf{(PUMP,OFF)}} \qquad \text{Eq. S6}$$

Using an appropriate detector, the two absorbances, one in pump presence and one in its absence, are measured as a function of varying time delays (t). During the experiment, the sample is continuously magnetically stirred to prevent it from any potential optical damage. Chirp correction is applied to the obtained spectral data to eliminate any effects of group velocity dispersion.

Optical Pump Terahertz Probe (OPTP) spectroscopy setup:

A Newport Terahertz time-domain spectrometer was used for mobility computations.[16] The THz-TDS spectrometer is powered by a Ti: Sapphire regenerative amplifier-based femtosecond laser system (Astrella, Coherent systems), which has also been utilised for ultrafast Transient Absorption spectroscopy investigations. The probe beam from the main laser system is directed into a THz spectrometer, which is then divided into two beams: gate and THz. The spectrometer utilised here relies on the usual approach for THz creation that is based on two-color laser-induced plasma formation. Nirvana Auto-Balanced Optical Receivers are used to do the detection. The optical pump beam (the one acquired from Opera SOLO, as indicated in the transient absorption setup) is kept substantially bigger than the THz probe beam diameter to achieve homogeneous probing of the photoexcited material.

THz TDS and time resolved THz spectra of Cs_2SnI_6 NCs were acquired at room temperature in the frequency range of 0.1–3 THz. Following the excitation of the NCs, the transmitted THz waves are measured at particular pump-probe time delays. Samples are spin coated on a quartz substrate with a thickness of 9μm for THz-TDS and TRTS experiments. THz-TDS software is used to collect the data, and it was afterwards utilised to analyse it.

15. Terahertz measurement details

While carrier density and relaxation control TA dynamics, time resolved photoconductivity (σ) dynamics derived from optical pump THz probe OPTP measurements are proportional to the product of carrier population (n) and short range effective mobility φμ (φ is the photon to free carrier conversion ratio):[24,6]

$$\sigma = n.\, e.\, \varphi\mu \ldots\ldots\ldots\ldots\ldots\ldots \quad \text{Eq. S7}$$

The OPTP investigations fundamentally record the pump induced relative attenuation of the terahertz electric field i.e. -ΔE/E. The instantaneous photoconductivity of the sample is further linearly proportional to this relative change -ΔE/E (t_p) in the thin film approximation as apparent from the following equation: [17]

$$\Delta\sigma(t_p) = \frac{\varepsilon_0 c(n_a+n_b)}{d}\left[\frac{-\Delta E(t_p)}{E_0}\right]\ldots\ldots\ldots\ldots\ldots \quad \text{Eq. S8}$$

Here, ε_0 is the permittivity of the free space, η_a and η_b are the refractive index of air and quartz (substrate) respectively, c is the speed of light in vacuum, d is the film thickness, $\Delta E = E_{pump} - E_0$ and E_{pump}, E_0 are the transmitted terahertz pulse in the presence and absence of pump, respectively.[18,19] It can thus be stated from Eq.S5 and Eq.S6 that there is linear dependency prevalent among these three quantities -ΔE/E, σ and μ.

REFERENCES

1 G. Kresse and J. Hafner, *Phys Rev B*, 1993, **47**, 558–561.

2 G. Kresse and J. Furthmüller, *Comput Mater Sci*, 1996, **6**, 15–50.

3 G. Kresse and D. Joubert, *Phys Rev B*, 1999, **59**, 1758–1775.

4 G. Kresse and J. Furthmüller, *Phys Rev B*, 1996, **54**, 11169–11186.

5 Y. Kim, Z. Yang, A. Jain, O. Voznyy, G.H. Kim, M. Liu, L. N. Quan, F. P. García de Arquer, R. Comin, J. Z. Fan and E. H. Sargent, *Angew Chemie Int Ed*, 2016, **55**, 9586–9590.

6 J. P. Perdew, K. Burke and M. Ernzerhof, *Phys Rev Lett*, 1996, **77**, 3865–3868.

7 A. Togo and I. Tanaka, *Scr Mater*, 2015, **108**, 1–5.

8 A. Togo and I. Tanaka, 2018, <cond-mat > arXiv:1808.01590

9 A. V Krukau, O. A. Vydrov, A. F. Izmaylov and G. E. Scuseria, *J Chem Phys*, 2006, **125**, 224106.

10 V. Wang, N. Xu, J.-C. Liu, G. Tang and W.-T. Geng, *Comput Phys Commun*, 2021, **267**, 108033.

11 M. Rasukkannu, D. Velauthapillai and P. Vajeeston, *Mater Lett*, 2018, **218**, 233–236.

12 A. E. Maughan, A. M. Ganose, M. M. Bordelon, E. M. Miller, D. O. Scanlon and J. R. Neilson, *J Am Chem Soc*, 2016, **138**, 8453–8464.

13 T. Li, X. Zhao, D. Yang, M.H. Du and L. Zhang, *Phys Rev Appl*, 2018, **10**, 41001.

14 A. Liu, H. Zhu, Y. Reo, M.-G. Kim, H. Y. Chu, J. H. Lim, H.-J. Kim, W. Ning, S. Bai and Y.Y. Noh, *Cell Reports Phys Sci*, 2022, **3**, 100812.

15 J. Yang, X. Wen, H. Xia, R. Sheng, Q. Ma, J. Kim, P. Tapping, T. Harada, T. W. Kee, F. Huang, Y.B. Cheng, M. Green, A. Ho-Baillie, S. Huang, S. Shrestha, R. Patterson and G. Conibeer, *Nat Commun*, 2017, **8**, 14120.

16 S. Mondal, R. Aepuru, J. Dana, N. Ghorai and H. N. Ghosh, *J Phys Chem C*, 2018, **122**, 28497–28505.

17 G. Kapil, T. Ohta, T. Koyanagi, M. Vigneshwaran, Y. Zhang, Y. Ogomi, S. S. Pandey, K. Yoshino, Q. Shen, T. Toyoda, M. M. Rahman, T. Minemoto, T. N. Murakami, H. Segawa and S. Hayase, *J Phys Chem C*, 2017, **121**, 13092–13100.

18 S. Guo, Q. Zhang, R. Sa and D. Liu, *Comput Theor Chem*, 2022, **1209**, 113609.

19 F. Guo, Z. Lu, D. Mohanty, T. Wang, I. B. Bhat, S. Zhang, S. Shi, M. A. Washington, G.-C. Wang and T.M. Lu, *Mater Res Lett*, 2017, **5**, 540–546.

20 S. Rieger, B. J. Bohn, M. Döblinger, A. F. Richter, Y. Tong, K. Wang, P. Müller-Buschbaum, L. Polavarapu, L. Leppert, J. K. Stolarczyk and J. Feldmann, *Phys Rev B*, 2019, **100**, 201404.

21 S. Lee, Y. Wang, Y. Liu, D. Lee, K. Lee, D. C. Lee and T. Lian, *Chem Phys Lett*, 2017, **683**, 342–346.

22 O. Flender, J. R. Klein, T. Lenzer and K. Oum, *Phys. Chem. Chem. Phys.*, 2015, **17**, 19238–19246.

23 X. Shen, S. Wang, C. Geng, L. Li, E. Zhao, J. Sun, W. Wu, L. An and K. Pan, *J Phys Chem C*, 2021, **125**, 5278–5287.

24 K. Justice Babu, G. Kaur, A. Shukla, R. Saha, A. Kaur, M. Sachdeva, D. K. Yadav and H. N. Ghosh, *ACS Photonics, 2022, **9**, 3, 969–978*.